2006

Computational hyperspectral interferometry for studies of brain function: Proof of concept

Douglas J. Fox
Washington University School of Medicine in St. Louis

Hana T. Velde
Washington University in St Louis

Chrysanthe Preza
Washington University in St Louis

Joseph A. O'Sullivan
Washington University in St Louis

William H. Smith
Washington University in St Louis

See next page for additional authors

Computational hyperspectral interferometry for studies of brain function: proof of concept

Douglas J. Fox, Jr., Hana Tysver Velde, Chrysanthe Preza, Joseph A. O'Sullivan, William H. Smith, and Thomas A. Woolsey

Hyperspectral interferometric microscopy uses a unique combination of optics and algorithm design to extract information. Local brain activity rapidly changes local blood flow and red blood cell concentration (absorption) and oxygenation (color). We demonstrate that brain activity evoked during whisker stimulation can be detected with hyperspectral interferometric microscopy to identify the active whisker–barrel cortex in the rat brain. Information about constituent components is extracted across the entire spectral band. Algorithms can be flexibly optimized to discover, detect, quantify, and visualize a wide range of significant biological events, including changes relevant to the diagnosis and treatment of disease.

OCIS codes: 100.0100, 100.2000, 100.2960, 170.4580.

1. Introduction

Different objects in a scene (images) are distinguishable based on intensity, contrast, texture, and color. Color is used in many scientific disciplines (biology, geology, agriculture, etc.) to identify objects (vessels, minerals, crops, etc.) related to components (hemoglobin, iron, chlorophyll, etc.). Spectral signatures often identify detailed information about a scene that is not available from conventional imaging with limited passband filters and may span absorption and radiation from the near-infrared to the ultraviolet regions.[1] Specific passband filters have long been employed to characterize different objects in images illuminated with white light. Different spectral components in a scene can be studied by capturing multiple images by quickly changing filters[2] or by simultaneously using multiple cameras with different filters.[3] In contrast to these approaches, it is possible to image multiple spectral components simultaneously by multispectral and hyperspectral sensing. Hyperspectral sensors have been used for remote sensing of vegetation, minerals, and manmade objects on the Earth and on Mars to make inferences about surface structure and to visualize contamination of food crops.[4]

Rats and many other animals have well-developed whiskers that they actively move during exploration of their environment. Information from the whiskers is analyzed by distinct groups of neurons at various levels of the nervous system that are arranged in patterns like that of the whiskers on the animal's face.[5,6] In the cerebral cortex these cells are in the middle or 4th cortical layer and are termed barrels. Numerous physiological experiments have shown that these neuron groups, which can be seen by simple histology, respond most vigorously to movements of the appropriate whisker.[7] A barrel in the cortex responds best to movement of the homologous whisker on the opposite face. Whisker stimulation also evokes activity-related changes in blood flow that can be detected by optical imaging; the resulting signal is called the intrinsic optical signal (IOS).[8–10] It is a straightforward matter to stimulate any or all of the whiskers in a highly controlled way, to record electrical and IOS changes, and to relate these changes to brain anatomy.

We studied the whisker–barrel system of adult rats to test whether we could record the full spectra by hyperspectral imaging in two dimensions from the surface of the rat brain at rest and during mechani-

D. J. Fox, Jr., and T. A. Woolsey are with the Department of Neurological Surgery, School of Medicine, Washington University, Box 8057, 660 South Euclid Avenue, St. Louis, Missouri 63110. H. T. Velde and W. H. Smith are with the Department of Earth and Planetary Sciences, Washington University, Box 1169, 1 Brookings Drive, St. Louis, Missouri 63130. C. Preza and J. A. O'Sullivan (jao@ee.wustl.edu) are with the Department of Electrical and Systems Engineering, Washington University, Box 1127, 1 Brookings Drive, St. Louis, Missouri 63130.

Received 6 September 2005; revised 4 January 2006; accepted 13 January 2006; posted 13 January 2006 (Doc. ID 64141).

0003-6935/06/133009-13$15.00/0

cal stimulation of the whiskers. Further we asked whether, to a first approximation, the analysis of these data would resemble those taken optically using passband filtering, which is now standard for detecting the IOS. The surface of the brain was imaged through the thinned skull and the membranes (meninges) that cover the brain. Green and orange filters that emphasize the absorption of total hemoglobin (Hbt) and deoxyhemoglobin (Hbr), respectively,[11] were used. Passband data were collected and processed by using variants on published protocols. The same animals were then scanned with a digital array scanned interferometer (DASI) through the same optics. These images were processed by using two different approaches to see whether the data that are detected by passband filtering can be extracted from the full spectral images computed from the measured interferograms. The first approach is a digital approximation of the passband filters. For the second, rather than filter the data, the spectra are separated into components. The resulting component images are computed by using all the spectral samples. The components used in the analysis are extracted automatically from the images. These components are interpreted as reflectance spectra, and we analyze the relationship of these spectra to the known absorption spectra of oxyhemoglobin (HbO_2) and Hbr.

The paper is organized as follows. We present a brief background on the imaging sensor and the biomedical application of interest in Section 2. In Section 3 we summarize the experimental methods for the sample preparation and data collection. The three different methods of image analysis are also described in Section 3. Results from the two imaging modalities and three imaging methods are compared qualitatively and quantitatively in Section 4. The results are discussed in Section 5.

2. Background

A. Digital Array Scanned Interferometer

The DASI was developed through many collaborations[4,12,13] and was patented by Smith.[14] The DASI measures the interferogram of each location along a slit corresponding spatially to a line. A data cube is obtained by a push-broom technique of sweeping the slit across a spatial region. The spectrum at each location along the slit may be estimated by computing the inverse Fourier transform of each interferogram. While two-beam interferometry has a long history, it became a practical spectroscopic method only by use of the digital fast Fourier transform (FFT). The DASI has many properties in common with the two-beam interferometer, but it has no internal moving parts. The sensor can be compact, low mass, and optically fast, all of which permit its application in diverse settings and extreme conditions. A hyperspectrometer can produce voluminous data that typically require digital processing to extract useful information. DASI data require destretching,[15] normalization, and FFT as preprocessing computations for many applications.

At a fundamental level, the performance of the DASI for estimating a hyperspectral data cube is limited by the data-collection methodology. A finite number of samples of the interferogram plus a background are measured. These samples are quantized in the detector plane. Quantitative assessments of resolution, aliasing, and signal-to-noise-ratio (SNR) issues, as determined by system parameters (including sensor optics, focal-plane array, and incident light intensity), are discussed in detail by Smith and Schempp.[13]

A measured hyperspectral data cube is usually modeled as having a spectrum at a spatial location. The spectrum at a given location depends on the total and the relative concentrations of substances there. Linear end-member analysis models this spectrum as a linear combination of constituent spectra, one spectrum for each substance in the scene. Inference about scene composition turns into inference about the constituent spectra and their concentrations. If the spectra themselves are not known, then this problem falls within the domain of components analysis, for which there are many alternatives. Motivated directly by the nonnegativity of spectra and their concentrations, and indirectly by the fact that optical sensors fundamentally count photons, we use a particular version of components analysis referred to in the literature as either nonnegative matrix factorization[16] or information-value decomposition[17] to infer both the components and their concentrations. The component spectra are inferred from a subset of the data and are then fixed for use in all data cubes. The data determine the optimal constituent spectra and their concentrations, as opposed to fixing the components based on prior knowledge. One advantage of this method is that any residual modulation due to the optical transfer function of the system (after calibration) is automatically accounted for in the analysis.

B. Biomedical Background

In medicine and biomedical research, different imaging modalities are increasingly used to monitor normal and abnormal structures and functions in living organisms and patients. The development of modern medicine is the direct result of the accurate description and illustration of human anatomy. From the late 1800s, structural information has been obtained from living organisms by x rays.[18] Subsequently, radio-opaque contrast that would reveal particular structures and their function[19–21] and improved optical methods without stains[22,23] or with specific nontoxic dyes[24] were developed. In the latter part of the twentieth century methods based on localization of different molecules labeled with radioisotopes and nuclear magnetic-resonance characteristics were brought into the imaging realm by development of new advances in instrumentation and data processing.[25,26]

An area of particular focus has been brain function. The systematic correlation of symptoms and signs with disease and trauma is related to changes in the function of specific brain structures that are demonstrated by direct electrical stimulation and recording of electrical changes from the brain.[27–29] Such data have increased our understanding of the localization

of different functions, such as vision, hearing, and memory, to specific brain regions. Localized electrical events result in localized changes in metabolic and circulatory events.[30] Strategies that permit imaging phenomena correlated with concomitants of brain activity, particularly changes in local blood flow, energy metabolism, and O_2 utilization, have greatly expanded investigations of brain function.[31–33]

Over the past decade we, along with other neuroscientists, have used narrowband illumination (passband) of the surface of the rodent brain to record the so-called IOS.[34] First formally described by Grinvald *et al.*,[35] IOS reflects changes in the optical properties of the brain when neurons are discharging. The bulk of the optical changes at the brain surface that can be viewed directly are related to flow-related changes in red blood cell (RBC) distribution and concentration as well as to hemoglobin oxygenation. Different workers use different illumination spectra to isolate different components of the IOS response for both experimental and practical reasons. Malonek and Grinvald provided data on changes in the spectra from a (one-dimensional) slit over time in response to physiological activation of the brain.[36] They observed that in the earlier phases of neural activity, absorption spectra consistent with Hbr, were better correlated spatially with the regions of changing neural activity than were those consistent with HbO_2. The original one-dimensional observations of different spectral components were made simultaneously. For two-dimensional imaging, current strategies involve serial imaging with different optical passband filters to collect data from different parts of the spectrum for the computations used to evaluate functionally related changes.[8] There could be a significant advantage to recording full spectra for simultaneous evaluation of different underlying components (i.e., HbO_2, Hbr, and Hbt), especially when there are constraints in certain experimental and clinical settings (emergencies, endoscopy, surgery, movement, etc.).

3. Methods

A. Experimental Methods

Animals. Animal housing, care, and experimental protocols met or exceeded standards of the National Institutes of Health, (NIH), Association for Assessment and Accreditation of Laboratory Animal Care International, and Washington University's Institutional Agricultural Animal Care and Use Committee. Female 250–350 g Wistar rats were sedated with 0.5 mg/kg of ketamine and 0.2 mg/kg of xylazine and were anesthetized with 0.5 g/kg of urethane. Animals respired spontaneously, and a core temperature of 37 °C was monitored with a rectal probe and was maintained with a thermal blanket.

Cranial window. After a midline incision, the scalp was reflected to expose the left side of the skull. A 3 mm square brass rod was glued to the right temporal bone by using cyanoacrylate. The skull over the right cerebral cortex was thinned with a dental drill and was covered with mineral oil and a coverslip [see Fig. 3(a) below]. The head was positioned to level the coverslip.

Whisker stimulation. All whiskers on the right side of the face were inserted into a small piece of fine-mesh window screen attached perpendicularly to a wand that was attached to a small solenoid. The screen was positioned parallel to and 5 mm from the skin surface on the rat's face. Care was taken to make sure that the whiskers were not bent (under tension at rest). Data-acquisition sequences were scripted on a Pro4, four-channel timer–controller (World Precision Instruments). This triggered a Pulsemaker A300 stimulator (World Precision Instruments) to generate 50 ms square-wave pulses at 5 Hz that drove the solenoid, which deflected the whiskers 5 mm from front to back. The Pulsemaker also triggered video capture on a Macintosh G3 computer (Apple Computer). The whiskers on the right face were stimulated at 5 Hz for 5 s prior to capturing images during the next 20 s as stimulation continued.

Image capture protocol. First, to verify activation based on optical filtering,[10] images were captured with an analog video camera in selected passbands illuminating the brain surface to yield images of barrel cortex with and without whisker stimulation. After video recording, the stimulation was repeated, and hyperspectral data were acquired at least three or more times. Then video recordings using optically filtered light were repeated to verify the persistence of activation.

Standard IOS capture. Illumination was from a 150 W, 21 V halogen MR-16 lamp with a dichroic reflector and a GX5.3 Bipin Base powered by a regulated power supply (Opti-Quip). Incident light intensity was increased with focusing units (Edmund Scientific) attached to ends of the light pipes. Green or orange optical filters were attached to the focusing units. For the green filter [Chroma Technology D540 25× (21.9 mm)], the absorption ratio for HbO_2:Hbr is 1.17. For the orange filter [Chroma Technology HQ620 60× (21.9 mm)], the absorption ratio for HbO_2:Hbr is 0.09. However, the absorption of Hbt under the green light is 5× that under the orange [see Fig. 2(a) below]. The image of the brain surface through the thinned skull was magnified (0.5×–3×) with a Nikon SMZ-U dissecting microscope (N.A. ≈ 0.13). The microscope was focused on surface vessels with white light prior to imaging (see Fig. 1; Nikon Corporation). Images were captured with a CCD camera (72S, Hamamatsu Corporation) at 30 Hz. Then 640 × 480 pixel images were stored digitally by using a real-time capture card (AG-5, Scion Corporation) in a Power Macintosh G3 computer running modified NIH Image 1.62 software.[10]

DASI sensor image capture. The DASI sensor was matched optically to an auxiliary port of the Nikon SMZ-U (Fig. 1). A match to the DASI focal plane was made by adding a lens to shorten the back focal length of the microscope. An achromat lens was selected to provide spatial resolution at the DASI focal plane similar to that obtained with the Hamamatsu CCD camera (Fig. 1). The entire positioning arm car-

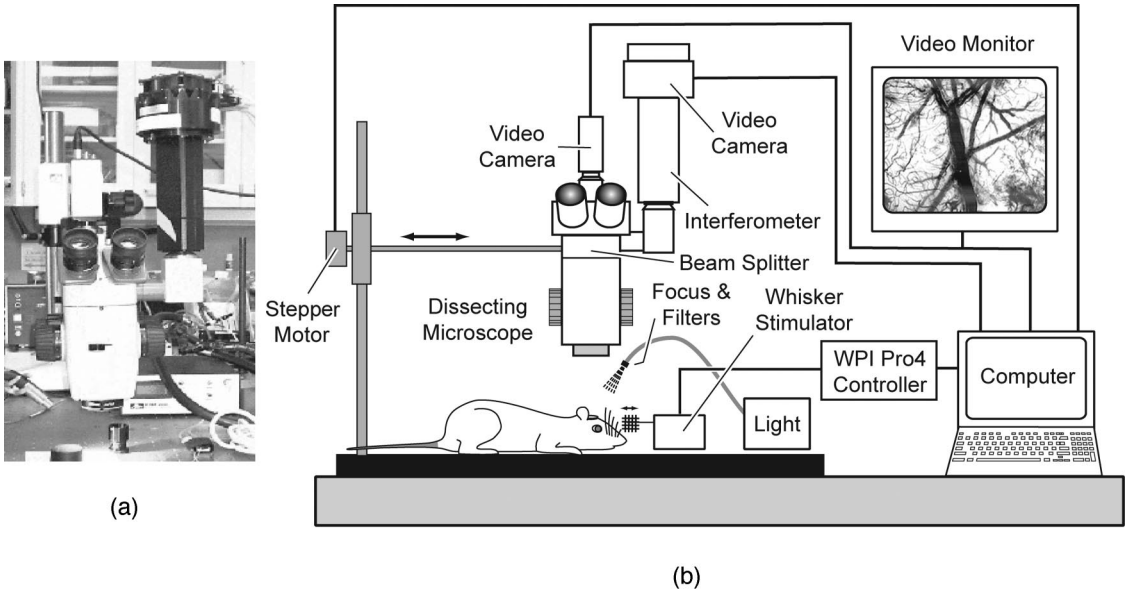

Fig. 1. (a) Photograph of the dissecting microscope with a CCD camera for standard video capture to the upper left and the hyperspectral interferometric microscopy sensor (DASI, the black attachment) to the upper right. (b) Schematic showing the optical, stimulating, recording, and analysis paths for the standard IOS recordings and for DASI capture. Video paths are directed to one or the other sensor by the beam splitter in the dissecting microscope. The entire apparatus is mounted on a Diagnostic Instruments (Sterling Heights) SMS20 boom stand microscope base. For image capture with the DASI, this was moved in 3 μm increments with a stepper motor. The drawing shows a rat with its head under the objective. The brain surface is viewed through the thinned skull that is covered with mineral oil and a coverslip. The brain is illuminated with focused white or passband filtered light. For video recordings, images are digitized and saved to a computer and can be analyzed within several minutes. For hyperspectral interferometry, the computer controls the stepper motor and data collection; images are processed off line. Physiological parameters (e.g., blood pressure and electrocardiogram are not shown) are recorded in the computer. The stimulator and programmed stimulus sequences are under computer control (WPI Pro4).

rying the microscope was moved at a 3 μm step resolution by coupling it to a stepper motor to scan the field of view. The spectral region of interest, 500–900 nm, was sensed with a firewire Dragonfly ICX084 CCD camera (Point Grey Research) with a 10-bit analog-to-digital (A/D) converter operating at 15 Hz, allowing a full scan of the exposed surface of the rat brain in ~2 s with a good SNR.

Histology. Following imaging, the animals were perfused transcardially with heparinized saline, followed by 4% paraformaldehyde in a 0.1 M phosphate buffer. The brains were removed and fixed by immersion in 4% paraformaldehyde in a 0.1 M phosphate buffer for 1–5 days, blocked, frozen with dry ice, and then sliced in a plane tangent to the brain surface at 150 μm on a sliding microtome. The slices were reacted for cytochrome oxidase (CO) activity,[37] and the sections were wet mounted by using Vectashield (Vector Laboratories). Surface sections showing pial arterioles, vessels, and deeper sections with holes from parenchymal arteriole veins were captured digitally at 2× by using an MTI CCD 72S camera (Dage-MTI Inc.) attached to a Nikon Labophot microscope (Seiler Instruments). The surface sections were matched to the *in vivo* image of the brain taken during optical imaging by rotating and scaling in x and y by using Adobe Illustrator SC (11.0.0) without warping (Adobe Systems; see Ref. 38 for schematic). The deeper sections were then added to the overlay by using the parenchymal vessels as fiducials. In this way the digital overlay represented an alignment of pial vessels, parenchymal arterioles, barrels, and optical image time courses.[6,38]

B. Image Analysis.

Standard IOS analysis. Each of the ten video clips were analyzed by using first-frame analysis. The prestimulus background absorption was subtracted from each frame of the 600-image movie before the video clips were averaged together. This yielded one 30 Hz, 20 s, 600-frame optical image sequence per stimulation period.[10] (For a fuller description of the details concerning image properties, statistics, and analyses, see "Data Analysis" on p. 355 in Ref. 10.)

Digital passband filtering. Interferometric data, measured by the DASI, were preprocessed by spectral and focal-plane calibration procedures.[15] A FFT brings the hyperspectral data into the spectral domain. Images corresponding to an arbitrary filtering of the spectra were computed digitally by taking the appropriate linear combinations of the images at the various spectra. For the optical passband filters green and orange in the standard IOS method described above, all images within the full width at half-maximum (FWHM) of a filter were summed. The passbands used are shown in Fig. 2(a). The resulting images are the digitally filtered images in Fig. 4 (shown below); images were computed at rest and during activation.

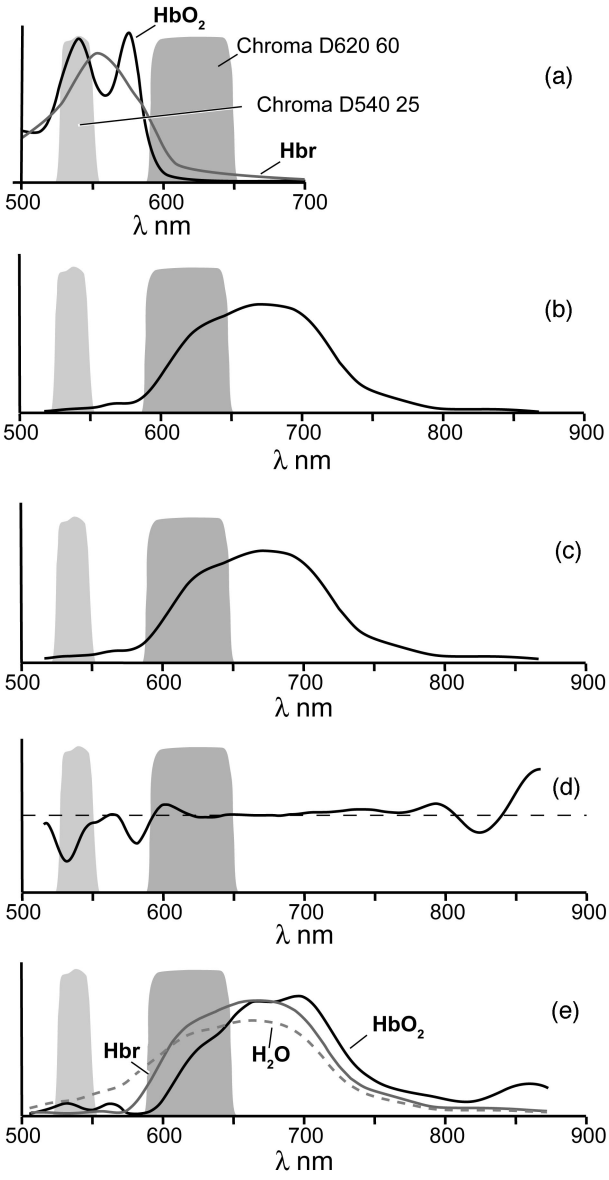

Fig. 2. (a) Linear, normalized absorption spectra (arbitrary linear scale) for oxyhemoglobin (HbO_2) and deoxyhemoglobin (Hbr) in solution[11] and smoothed filter passbands. For shorter wavelengths (green filter, 540 ± 12.5 nm), the Hbt absorption is at least 5 times greater than that for longer wavelengths (orange filter, 620 ± 30 nm). The green filter includes an isobestic point of the hemoglobin absorption spectra and is roughly equally sensitive to Hbr and HbO_2 (46% and 54%, respectively). The orange filter is ~4 times as sensitive to Hbr as to HbO_2 (78% and 22%, respectively). (Filter passbands are indicated in all panels.) (b) Relative spectral reflectance computed from data captured by DASI at baseline or rest. (c) Relative spectral reflectance with whisker activation computed from data captured by DASI. (d) Relative differences in the spectra shown in (b) and (c). While changes occur in the regions selected by the filter passbands, additional information is available from regions not passed by the filters. The dashed line indicates that there is no difference in reflectance between background and active images. (e) Components of the reflection spectra extracted from data captured by DASI. The three most significant spectral components extracted by end-member analysis are likely reflection related to water H_2O, HbO_2, and Hbr. The HbO_2 and Hbr curves are roughly the inverse of the corresponding spectra in (a).

Independent spectral component analysis. If spectral bands, optical characteristics of the sensor, and illumination are known beforehand, then, as described above, filters may be used to restrict the incoming light sequentially to each band. If spectra are not known ahead of time and must be extracted from the data, then the sensor must have good spectral sensitivity across all bands of possible interest. Given data collected across many bands, a components analysis must be run to determine the significant spectra and their relative contributions. There are several possibilities for the components analysis, including singular-value decomposition (and related principal components analysis) and various versions of independent components analysis.

The approach adopted here is referred to as either nonnegative matrix factorization or information-value decomposition. The following is a brief summary. More details are given in Appendix A.

Given a measured hyperspectral data cube with spectral samples

$$S(m,\ n,\ k), \quad 1 \le m \le M, \quad 1 \le n \le N, \quad 1 \le k \le K,$$

where m and n index the two spatial (image) directions and k indexes the spectrum sample, the goal is to find a data cube represented as a linear combination of constituents

$$A(m,\ n,\ k) = \sum_{l=1}^{L} u(m,\ n,\ l)d(l)v(k,\ l) \qquad (1)$$

that is as close to the measured data cube as possible. The number of spectral samples is typically in the hundreds, while only a few constituents are used in the linear combination. The spectral components $v(k, l)$ are nonnegative and sum to 1 over k. The concentration images $u(m, n, l)$ are nonnegative and sum to 1 over the spatial indices m and n. The weights $d(l)$ are nonnegative. To quantify the discrepancy between the measured data cube and its approximation, we use the information divergence (I divergence):

$$I(S \,\|\, A) = \sum_{m=1}^{M}\sum_{n=1}^{N}\sum_{m=1}^{K}\left[S(m,\ n,\ k)\ln\frac{S(m,\ n,\ k)}{A(m,\ n,\ k)} - S(m,\ n,\ k) + A(m,\ n,\ k)\right].$$

The I divergence is motivated by the nonnegativity of the data cubes, the nonnegativity of the constituents and their concentrations, the desire to weight all measurements equally, and the desire to have a rigorously justifiable discrepancy measure.[39–42] The resulting algorithm minimizes $I(S \,\|\, A)$ over all such decompositions.

The approach taken was as follows. First, a common spatial section of all data cubes was used to extract three spectral components $v(k, l)$, where $l = 1, 2, 3$. This computation is iterative; we anticipated implementation of this during a calibration

stage. These computations are run off line with iterations run until convergence (~200 iterations). Second, these components were analyzed to ensure that they were as independent as possible. Third, these components were fixed and then used to estimate both the corresponding concentration images $u(m, n, l)$ and the weights $d(l)$.

After computing the constituents, we conducted a comparison among them and the absorption spectra for HbO_2 and Hbr, yielding an interesting correspondence, as discussed below.

Image comparisons. Following analysis, the images collected in two ways through the same apparatus and analyzed in three ways were adjusted in Adobe Photoshop 8.0 (Adobe Systems Inc.) for intensity, contrast, size, and aspect ratios to permit direct visual comparisons. Because of differences in the data resolution and image analysis, qualitative comparisons among the various images are arguably more meaningful than quantitative comparisons. Furthermore, the images were collected from a living rat, so no independent, quantitative results are available. Nevertheless, some quantitative analysis among the resulting images is possible.

Since the digital filter and the components are computed from hyperspectral data, their outputs can be compared quantitatively. To do this, we view the linear combination [Eq. (1)] of these three extracted components as an estimate of the entire data cube. The hyperspectral data cubes are positive. The at-rest hyperspectral data cube analyzed here has a total sum of 8.57×10^{11}; of that, 57% is attributed to the water component, 39% to the HbO_2 component, and 4% to the Hbr component [Fig. 2(e) shows the three-component spectra]. For the at-rest images, the estimate of the green image from the components is obtained by using relative contributions of 0.85 for the HbO_2 component, 0.09 for the H_2O component, and 0.06 for the Hbr component. For the orange image, the estimate is obtained by using relative contributions of 0.40 for the HbO_2 component, 0.58 for the H_2O component, and 0.02 for the Hbr component. These fractions were used to compute the estimated data cube. The two digital filters were then used on this estimated data cube: a 2×3 matrix was used pixelwise to estimate the green and orange filter outputs for the at-rest and activated images. These estimated digitally filtered green and orange images were compared with the actual digitally filtered images (shown in the middle column of Fig. 4). For comparison, we computed the mean-square error between the actual and the estimated digitally filtered images and divided it by the total energy in the respective actual digitally filtered image. This yields a relative mean-square-error measure for image comparison.

4. Results

A. Spectra and Spectral Analyses

Figure 2(a) shows the known absorption spectra of HbO_2 and Hbr. Figures 2(b) and 2(c) show the spectra recorded under baseline and activated conditions, respectively. The differences are small, as is well known from IOS studies. These are summarized in Fig. 2(d). The changes are not confined to the passbands of the filters we use for IOS. Figure 2(e) shows the extracted spectra. The wavelength axis for the extracted spectra was calibrated by using four narrowband sources over the visible band. A linear fit between the estimated and the known center frequencies (equivalently, wavenumbers) yields the wavelengths indicated; we estimate a uniform error bar of ± 3 nm (0.5% at 500 nm to 0.3% at 800 nm). The light detected follows many optical paths with varying optical depths. Thus neither the absorption nor the reflectance spectra, nor a simple combination of them, fully characterizes the measured spectra. While a better model would involve a radiative transfer equation, the extracted spectra summarize the measured effects more simply and directly. Interestingly, extracted spectra have significant features (peaks and valleys) in the same 500–600 nm spectral band as the absorption spectra of HbO_2 and Hbr, providing additional confidence that they correlate with hemoglobin and blood oxygenation levels. Appropriately (as shown in the third column of Fig. 4 below), arteries and veins are emphasized in the top row, and veins are emphasized in the second row.

B. Anatomy

Images of the sections were aligned and stacked: surface [Fig. 3(c)] landmarks (vessels) were used to register the image data with CO staining patterns [whisker barrels, Fig. 3(d)] in the middle cortical layer that have a direct 1:1 relationship to the whiskers on the opposite face. These are outlined and identified according to standard nomenclature (A1, C2, E3) in Fig. 3(e).[43]

C. Imaging—Qualitative

Images from optically and digitally filtered images and from component analysis are compared in Fig. 4. The four panels in the left column (Optically Filtered) are images of the cortical surface (boxes on the sections in Fig. 3) captured with illumination at the green and orange wavelengths (540 ± 12.5 nm and 620 ± 30 nm, respectively). For the baseline, the green image shows all arteries (a) and veins (v) on the brain surface and the vessels (arteries and veins) in the overlying dura (d). The orange image at rest is relatively selective for Hbr in the draining surface and the dural veins. Stimulating the whiskers results in absorption changes over the activated barrels as shown in the difference images (active minus baseline). With the green filter, absorption increased (darker) in the active brain, which is consistent with known increases in capillary perfusion and red blood cell (RBC) concentration. The feeding arteries are outlined because they dilate. With the orange filter, veins draining activated cortex are bright because the absorption due to Hbr is reduced. The image is typical of the later phases during whisker stimulation, when there is a local increase in blood flow (hyperemia).

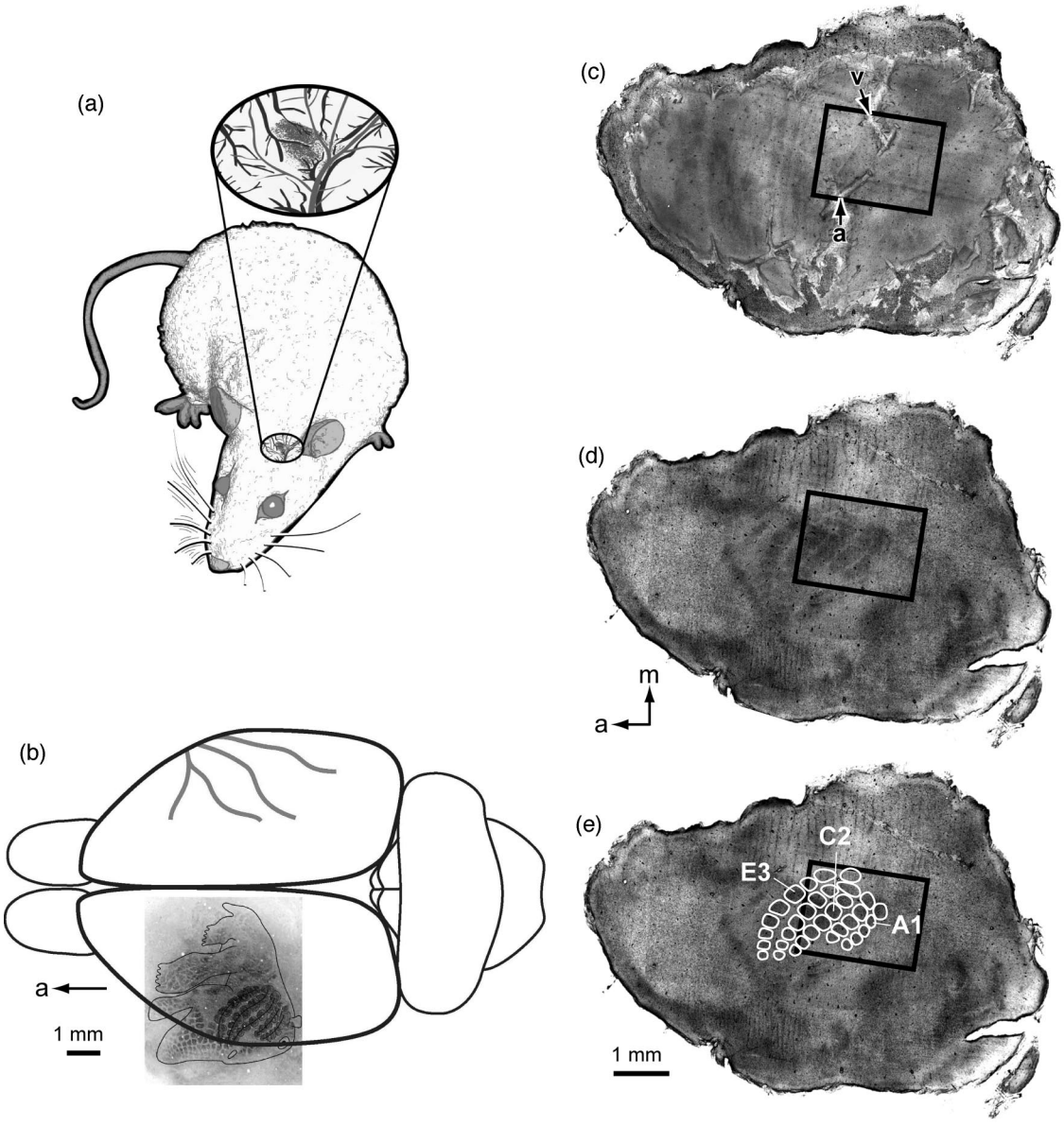

Fig. 3. (a) Drawing of a rat with the surface of the whisker cortex shown through the thinned skull. When the right whiskers move, the left cortex is activated. (b) Sketch of the rat brain viewed from above, showing the main artery (middle cerebral) that supplies the whisker representation on the right cerebral hemisphere only (top). The outline of the rat's body map (anatomical and functional) is drawn on a photograph of a histological section stained for the activity of the mitochondrial enzyme CO as scaled and placed over the left hemisphere (bottom). The image extends beyond the brain outline because it represents a view that unwraps the curved cortical surface. Patches of nerve cells (barrels) define regions of inputs from the whiskers on the opposite face. The arrow points toward the nose (a = anterior). (c) Composite stack of histological sections (stained for activity of the mitochondrial enzyme CO), including the brain surface used to align vessels (arteries, a; veins, v) visualized during video recording with tissue markers found 500 μm under the surface. The box here and in (d) and (e) indicates the location of the images in Fig. 4. (d) Dark-staining CO patches show the location of the representations of different whiskers on the opposite face. (e) Individual barrels are circled to show the match with different images displayed in Fig. 4. Compass: a, anterior (nose); m, medial (toward the midline) gives the orientation for (c)–(e).

That is, the veins are redder because the concentration of HbO_2 is increased and Hbr is washed out.[44]

Digitally filtered images that mimic the green and orange filters are shown in the middle column of Fig. 4. The baseline images are remarkably similar to those taken with the physical filters. That is, the green image shows arteries and veins equally well. (The image has poorer spatial resolution because of lower pixel density and depth.) The same is true for the derived orange image except that the artery is less prominent. For the difference images (Active-Baseline) the derived images are much less comparable to the optically filtered images. The arteries in the derived green image are prominent, which is consistent with the dilation seen in the filtered image. The brain surface may be darker but not strikingly

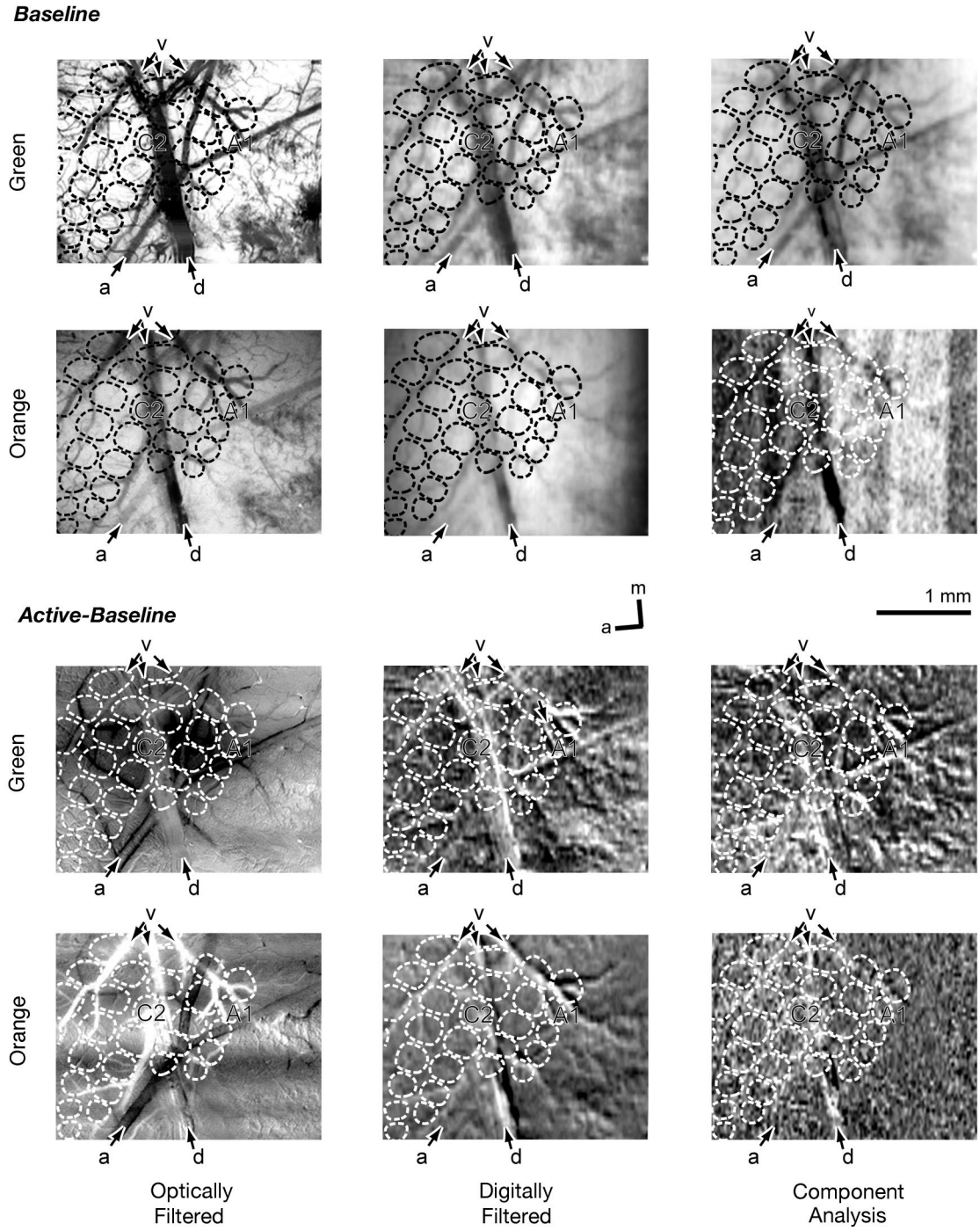

Fig. 4. Imaging Results. The surface of the left hemisphere of the rat brain visualized through the thinned skull. Arteries (a) and veins (v) on the brain surface and in the covering membrane (in the dura mater, d) are prominent. Images are arranged in two functional groups (Baseline and Active Baseline) by the three different imaging modalities (Optically Filtered, Digitally Filtered, and Component Analysis) and by the spectra used (Green and Orange). Optically filtered images were collected with illumination through green and orange filters. Digitally filtered images were processed with software filters designed to mimic the optical filters applied to hyperspectral data [Fig. (2a)]. Component analysis images were based on spectral signatures of major components [Fig. (2e)]. For each image the anatomical regions defining the whisker representations in the histological sections (Fig. 3) are outlined. The baseline (at-rest) images are remarkably similar for all three approaches. With whisker stimulation the strong changes in the optically filtered images are partially suggested in the digitally filtered and component analysis images. See text for details and consideration of similarities and differences among the three different methods of emphasizing image components. Compass: m, medial; a, anterior.

so. In the derived orange image the arteries are much less prominent, while the veins are more so. The latter are bright in several places and shadows are prominent (see Section 5).

The components analysis method extracted three basis spectra, as shown in Fig. 2(e). The images from two of these are shown in the first and second rows of the right column (labeled Component Analysis) of Fig. 4. Interestingly, while these spectra were extracted automatically, they are similar in many respects to HbO_2 green and Hbr orange in the baseline optically and digitally filtered images. Some differences are important; i.e., the veins are relatively lighter in the green image, while the arteries are bright in the orange image. This suggests that the components extracted may be specific to different forms of Hb, because they evaluate information from the full spectrum [see Fig. 2(a)]. Difference images (Active-Baseline) from the component analysis, as the digitally filtered images, have low spatial resolution and small misregistrations. This is expected, as they are extracted from the same data set as the derived images. Nevertheless, the extracted image is darker in the same locations as in the optically filtered image, while the orange extracted image is brighter, coinciding with both the veins in the optically filtered image and the active barrels, as the brain tissue is also brighter.

D. Imaging—Quantitative

The three columns of Fig. 4 show the results of three different types of analysis, with the second and third column computed from the same underlying data. The component images shown in the third column are not directly comparable with the filter outputs in the first two columns. Compared with the second column, the video system used to compute the filtered images in the first column used substantially more data, collected at a higher resolution. For these reasons, the qualitative comparisons among them are arguably more meaningful than quantitative comparisons. Furthermore, the images were collected from a living rat, so no independent, quantitative results are available.

Nevertheless, some quantitative analysis between the resulting images is both possible and informative. For the at-rest green image, the relative mean-square error between the approximate digitally filtered image, computed as described in Subsection 2.B, and the digitally filtered image in the second column of Fig. 4 is 0.0045 (23.5 dB). For the at-rest orange image, the resulting relative mean-square error is equal to 2.1×10^{-4} (36.8 dB). The numbers for the activated images are nearly identical. Thus the three components capture most of the interesting signals for the purpose of analyzing brain activity. Also, since the components can be used to compute the green and orange filtered images with low error, they provide at least as much information as those filtered images.

We examined the mean-square-error images between the digitally filtered images and those obtained from the components. A qualitative observation is that the error in the green images is uncorrelated with the underlying biology, while the error in the orange images is correlated with the underlying biology. In particular, the error in the veins is extremely low. This observation merits more detailed analyses in future studies.

5. Discussion

The objective of the present study was to determine whether hyperspectral interferometry can be adapted to evaluate biomedical questions. We tested this hypothesis in a biological context that is well known and understood, namely, blood distribution in the resting brain and flow-related changes with sensory stimulation. The whisker–barrel system of rodents (in this case the rat) offers a number of advantages for such an evaluation (see Fig. 3). (1) Rats are standard subjects for laboratory studies; (2) the whiskers are important in the animal's behavior and are easily stimulated in a controlled fashion; (3) the brain areas that process the whisker inputs are clearly delineated and accessible and provide accurate landmarks for accurately relating data obtained in different ways from the same subject and across subjects; and (4) the whisker–barrel system has been widely studied in imaging to detect the IOS since the approach was first discovered.[35,45]

Digital filtering mimics optical filters by extracting data from the spectral ranges of the optical filters (see Fig. 2). Qualitatively the data obtained in the resting condition by digital filtering closely resembles that of the optical filters. For the green filter, both methods show the location of RBCs in arteries and veins that are of roughly equal intensity; for the orange filter, the veins are more prominent in both methods, which is consistent with the increased Hbr at rest [see Fig. 2(a)]. The component analysis under baseline conditions is similar but not the same. In particular, as shown in Fig. 4, in the image labeled green, the arteries are relatively more prominent than are the veins in comparison to the filtered images. In the orange component analysis image, the veins are more prominent and the arteries are no longer dark in contrast to the optically or digitally filtered images. This is consistent with the interpretation that the components computed from the full spectrum actually correspond to HbO_2 and Hbr.

Difference images (Active-Baseline) show changes in appropriate portions of the field of view. For the optically filtered images (Fig. 4, left column), these are consistent with the results reported by many investigators. Namely, with the green filter, there are changes in feeding arteries (they dilate, hence the outline) and RBC concentration increases in the brain owing to increased perfusion and a consequent local increase in RBC concentration (hematocrit) localized to the appropriate region—the whisker barrels that are activated by whisker stimulation.[34] The veins draining these barrels, but not other cortex, appear bright under the orange filter. This is

consistent with the overall decrease in the concentration and volume of Hbr after the first seconds of stimulation related to increased blood flow (hyperemia). Changes in the digitally filtered and component analysis difference images are much less pronounced. In the green images there are strong shadows related to the middle cerebral artery that are consistent with the dilation seen in the optically filtered images. Less obvious but suggestive is a darkening related to the activated barrels, but these changes are not dramatic. In the orange digitally filtered image the shadows are associated with veins draining the barrels. In the component analysis orange image the localization of the bright veins more closely matches those in the optically filtered orange image, and interestingly the overall region is slightly brighter (Fig. 4).

The DASI difference images either digitally filtered or analyzed for components showed less pronounced changes than did the optically filtered images. There are several possible reasons for this, all of which can be addressed by equipment upgrades and adjusting procedures. For one thing, the images are clearly courser (pixelated). This reflects differences in the final magnifications of the images detected by the video (higher) and DASI (lower) CCDs. We are currently modifying the optics to eliminate these differences. For another, changes in HbO_2, Hbr, and Hbt with normal brain activation are known to be fairly small.[34] In fact a characteristic of all approaches to IOS studies is devising ways to increase the SNR, principally by averaging multiple samples (images). Here the DASI capture scanned the brain only three or four times in each polarizer orientation. In this regard, the findings suggest that the data collected by DASI can be more robust and therefore, with optimized hardware and software, could be acquired in less time than with standard video processing. If this is true, then the potential exists to follow a wider range of dynamic processes in the brain or in other systems with an optimized (see below) system.

The second column of Fig. 4 demonstrates that digitally filtering the hyperspectral data cubes (following the digital filters described in Section 2 and Fig. 2) yielded images that are very similar to images collected by using an optical filter. This provides an alternative method for measuring the IOS. However, this method is much more flexible in that a virtually infinite set of arbitrary digital filters may be used to extract pertinent signals. Equally important, the hyperspectra may be separated into constituent spectra as described in Section 3 and shown in Fig. 2. The constituent spectra may be fixed prior to the measurements or may be extracted from the measurements themselves. The use of fixed spectra may be motivated by a desire to incorporate known prior information about spectra into a scene or as a result of a calibration procedure. However, it is often better to extract the constituent spectra from the measurements if there are unknown or varying attenuations in the optical path or if there are unknown or varying biological agents in the scene. In the latter case, the approach described here for component analysis yields the spectra of the underlying constituents and their relative concentrations. We used this method as described in Section 3, extracting the constituents from a spatial subset (11 columns, each of length 300, from each of 2 at-rest data cubes and 3 activated data cubes, and then used these extracted spectra to extract the relative concentrations of all data cubes (see Figs. 2 and 4).

One of the most interesting results from this approach is that, with no assumptions and without reference to prior spectral information, we derived spectral images that closely resembled the images expected for water, Hbr, and HbO_2. The importance of this result is easily understood. Spectral features of hemoglobin in diverse living media will necessarily be variable since these spectra are dependent on the living environment and the optics of the conditions under which the measurements are obtained. Thus an iterative fitting of data to reference spectra from a database will contain errors that arise from the forced fit and are likely to vary from measurement to measurement as well as from animal to animal. Determining major components from the data is a powerful tool that can continue to be characterized and made more robust. The determination of scene components from the data also reveals a means to acquire specific spectral data that are optimized for selectivity and allows the quantitative characterization of the nature of the spectral changes being sensed. Further, if the observed scene (i.e., an animal or human brain) exhibits unusual or even unknown spectral features, these will be detected, since reference to an existing database of the spectra is not implied. One point for further investigation, then, is to define those circumstances in which a simple multispectral image with well-defined passbands is preferred and those in which a hyperspectral image is preferred. These choices are not mutually exclusive.

One early hope was that IOS could be used to guide neurosurgical procedures intraoperatively. Given that the spatial resolution and the extensive field-of-view optical approaches permit the assessment of the exposed brain, considerable effort has been put into adapting existing IOS technology to the operating theater.[46–48] At present, this technology is not widely used. An approach such as the one we have explored could offer advantages for intraoperative brain mapping and other studies of the exposed human brain. The component analysis of these images has particular appeal. As illustrated in Fig. 4, the differentiation of what is likely HbO_2 from Hbr by using the full spectrum indicates that (a) more information is available to characterize a change or difference and (b) as in other applications for this approach scene segmentation for feature recognition could be more definitive. In addition to the advantage of speed, optical approaches that avoid contact with the brain directly avoid potential brain injury. However, in addition to assays of brain function, there are other good reasons

for believing that the technology we are developing could be used to identify other processes that are disease related, regardless of the tissue or organ, based on the identification and recognition of optical signatures that can be analyzed from full spectral images[22] similar to those documented for crops, minerals, and other features.[4] A single DASI instrument could collect any spectral information in almost all settings. Such an instrument would not be dependent on selection of the inputs, as is the case with optical filters, but rather could permit continuous refinement and testing on the same image by the unbiased extraction and representation of the components of interest. With faster computers and state-of-the-art imaging hardware, the use of this technology, virtually in real time, is plausible.

An ultimate goal of this research is to accurately and efficiently identify spectral signatures for identification or optimized detection and quantification of significant changes that are small. We report our initial evaluation of hyperspectral sensing to characterize a physiological response in living animals. The results extracted in two fundamentally different ways are similar but not identical. The results (Fig. 4) clearly show that DASI capture and the two methods of analysis are very promising. Furthermore, there is considerable potential for improvement of the method and the general approach to this and other biomedical questions. Indeed it is likely that, with equipment optimized for this task, significant improvements in the general approach to IOS and other studies—investigatory and routine—that the approach can be both simple and expanded for use in other applications. Early quantitative assessment of the images described in the results initially for objective comparison of data evaluated by different methods (see the three columns in Fig. 4) indicates that such approaches will offer significant insight into the biological factors contributing to such images. But they also suggest that such strategies can be employed to assess and develop different quantitative approaches to the analysis of different resulting images (see the four rows in Fig. 4). These approaches clearly include processing that has strong theoretical bases (i.e., Ref. 49). And to a first approximation they are remarkably similar to images collected by standard IOS methods. Since the potential for refining acquisition and analysis of the information-rich multispectral images is enormous, these findings are an important proof of concept that lead to further investigation and development.

Appendix A. Computations of Components and Concentrations

The iterative algorithm is based on the variational representation of the I divergence as

$$
\begin{aligned}
I(S \,\|\, A) &= \sum_{m=1}^{M}\sum_{n=1}^{N}\sum_{k=1}^{K}\left[S(m,\,n,\,k)\ln\frac{S(m,\,n,\,k)}{\sum_{l=1}^{L}u(m,\,n,\,l)d(l)v(k,\,l)} - S(m,\,n,\,k) + \sum_{l=1}^{L}u(m,\,n,\,l)d(l)v(k,\,l)\right] \\
&= \min_{\Phi\in\prod}\sum_{m=1}^{M}\sum_{n=1}^{N}\sum_{k=1}^{K}\sum_{l=1}^{L}\left[\Phi(l|m,\,n,\,k)\mathrm{S}(m,\,n,\,k)\,\ln\frac{\Phi(l|m,\,n,\,k)S(m,\,n,\,k)}{u(m,\,n,\,l)d(l)v(k,\,l)}\right. \\
&\quad \left. - \Phi(l|m,\,n,\,k)S(m,\,n,\,k) + u(m,\,n,\,l)d(l)v(k,\,l)\right].
\end{aligned}
$$

This expression takes into account the component decomposition

$$A(m,\,n,\,k) = \sum_{l=1}^{L}u(m,\,n,\,l)d(l)v(k,\,l).$$

The minimization then alternates among Φ taking values in the set of probabilities

$$\prod = \left\{\Phi : \Phi(l|m,\,n,\,k) \geq 0, \quad \sum_{l=1}^{L}\Phi(l|m,\,n,\,k) = 1\right\}$$

and the three parts of the decomposition, $v(k, l)$, $u(m, n, l)$, and $d(l)$. Assuming initial estimates, the iterations proceed with (j) indexing iteration number as

$$\Phi^{j}(l|m,\,n,\,k) = \frac{u^{(j)}(m,\,n,\,l)d^{(j)}(l)v^{(j)}(k,\,l)}{\sum_{l=1}^{L}u^{(j)}(m,\,n,\,l)d^{(j)}(l)v^{(j)}(k,\,l)},$$

$$d^{(j+1)}(l) = \sum_{m=1}^{M}\sum_{n=1}^{N}\sum_{k=1}^{K}\Phi^{(j)}(l|m,\,n,\,k)S(m,\,n,\,k),$$

$$v^{(j+1)}(k,\,l) = \frac{1}{d^{(j+1)}(l)}\sum_{m=1}^{M}\sum_{n=1}^{N}\Phi^{(j)}(l|m,\,n,\,k)S(m,\,n,\,k),$$

$$u^{(j+1)}(m,\,n,\,l) = \frac{1}{d^{(j+1)}(l)}\sum_{k=1}^{K}\Phi^{(j)}(l|m,\,n,\,k)S(m,\,n,\,k).$$

The iterations proceed until convergence. To make the components as independent as possible, we added a relaxation penalty term, whose weight converges to zero asymptotically, thereby removing the penalty. This term is $\lambda^{(j)}\sum_{l=1}^{L}[\ln d(l) - d(l)]$ and is meant to separate the spectra to avoid overfitting the data. When the spectra $v(k, l)$ are fixed as described in Section 3, the iterations proceed as above, but without the iterations on $v(k, l)$. In our experience these iterations converge rapidly.[50,51]

We are especially grateful to Jeffrey Ojemann for his early encouragement and perspectives. Supported in part by National Institutes of Health grants NS28781 and NS49048 to T. A. Woolsey, an award to T. A. Woolsey from the Spastic Paralysis Foundation of the Illinois-Eastern Iowa District of Kiwanis International, and by separate support to T. A. Woolsey from the McDonnell Center for Studies of Higher Brain Function.

References

1. G. A. Swayze, R. N. Clark, A. F. H. Goetz, T. G. Chrien, and N. S. Gorelick, "Effects of spectrometer band pass, sampling, and signal-to-noise ratio on spectral identification using the Tetracorder algorithm," J. Geophys. Res. **108** (E9), 5105, doi: 10.1029/2002JE001975 (2003).
2. A. K. Dunn, A. Devor, H. Bolay, M. L. Andermann, M. A. Moskowitz, A. M. Dale, and D. A. Boas, "Simultaneous imaging of total cerebral hemoglobin concentration, oxygenation, and blood flow during functional activation," Opt. Lett. **28,** 28–30 (2003).
3. M. Ehlers, "Multisensor image fusion techniques in remote sensing," J. Photogramm. Remote Sens. **46,** 19–30 (1991).
4. P. D. Hammer, L. F. Johnson, A. W. Strawa, S. E. Dunagan, R. G. Higgins, J. A. Brass, R. E. Slye, D. V. Sullivan, W. H. Smith, B. M. Lobitz, and D. L. Peterson, "Surface reflectance mapping using interferometric spectral imagery from a remotely piloted aircraft," IEEE Trans. Geosci. Remote Sens. **39,** 2499–2506 (2001).
5. C. Welker and T. A. Woolsey, "Structure of layer IV in the somatosensory neocortex of the rat: description and comparison with mouse," J. Comp. Neurol. **158,** 437–454 (1974).
6. T. A. Woolsey and H. Van der Loos, "The structural organization of layer IV in the somatosensory region (SI) of mouse cerebral cortex: the description of a cortical field composed of discrete cytoarchitectonic units," Brain Res. **17,** 205–242 (1970).
7. D. J. Simons, G. E. Carvell, A. E. Hershey, and D. P. Bryant, "Responses of barrel cortex neurons in awake rats and effects of urethane anesthesia," Exp. Brain Res. **91,** 259–272 (1992).
8. A. Devor, A. K. Dunn, M. L. Andermann, I. Ulbert, D. A. Boas, and A. M. Dale, "Coupling of total hemoglobin concentration, oxygenation, and neural activity in rat somatosensory cortex," Neuron **39,** 353–359 (2003).
9. J. L. Dowling, M. M. Henegar, D. Liu, C. M. Rovainen, and T. A. Woolsey, "Rapid optical imaging of whisker responses in the rat barrel cortex," J. Neurosci. Methods **66,** 113–122 (1996).
10. J. Erinjeri and T. A. Woolsey, "Spatial integration of vascular changes with neural activity in mouse cortex," J. Cereb. Blood Flow Metab. **22,** 353–360 (2002).
11. W. G. Zijlstra, A. Buursma, and W. P. Meeuwsen-van der Roest, "Absorption spectra of human fetal and adult oxyhemoglobin, de-oxyhemoglobin, carboxyhemoglobin, and methemoglobin," Clin. Chem. **37,** 1633–1638 (1991).
12. P. D. Hammer, F. P. J. Valero, D. L. Peterson, and W. H. Smith, "Remote sensing of Earth's atmosphere and surface using a digital array scanned interferometer: a new type of imaging spectrometer," J. Imaging Sci. Technol. **36,** 417–422 (1992).
13. W. H. Smith and W. Schempp, "Digital array scanned interferometers," Exp. Astron. **1,** 389–405 (1991).
14. W. H. Smith, "Digital array scanned interferometer, U.S. patent 4,976,542 (11 December 1990).
15. D. R. Fuhrmann and W. H. Smith, "Empirical modeling and calibration of Fourier transform spectrometers I: linearization and normalization of interferograms," Opt. Eng. **42,** 2268–2276 (2003).
16. L. Hubert, J. Meulman, and W. Heiser, "Two purposes for matrix factorization: a historic appraisal," SIAM Review **42,** 68–82 (2000).
17. G. W. Fumas, S. Deerwester, S. T. Dumias, T. K. Landauer, R. A. Harshman, L. A. Streeter, and K. E. Lochbaum, "Information retrieval using a singular value decomposition model of latent semantic structure," in *Proceedings of the Eleventh Annual International Conference on Research and Development in Information Retrieval* (ACM Press, 1988), pp. 465–480.
18. "Wilhelm Conrad Röntgen—biography," in *Nobel Lectures, Physics 1901-1921* (Elsevier, 1967).
19. R. S. Ross, "Clinical applications of coronary arteriography," Circulation **27,** 107–112 (1963).
20. F. M. Sones, Jr., E. K. Shirey, W. L. Proudfit, and R. N. Westcaott, "Cine-coronary arteriography," Circulation **20,** 773 (1959).
21. E. A. Graham, W. H. Cole, and G. H. Copher, "Visualization of the gallbladder by the sodium salt of tetrabromophenophthalien.," JAMA, J. Am. Med. Assoc. **82,** 1777–1778 (1924).
22. P. Asawanonda and C. R. Taylor, "Wood's light in dermatology," Int. J. Dermatol **38,** 801–807 (1999).
23. J. Niamtu, "Digitally processed ultraviolet images: a convenient, affordable, reproducible means of illustrating ultraviolet clinical examination," Dermatol. Surg. **27,** 1039–1042 (2001).
24. F. N. Joudi and B. R. Konety, "Fluorescence cystoscopy and bladder surveillance," Curr. Opin. Urol. **14,** 265–270 (2004).
25. M. M. Ter-Pogossian and H. N. Wagner, Jr., "A new look at the cyclotron for making short-lived isotopes," Nucleonics **24,** 50–62 (1966).
26. S. Ogawa, T. M. Lee, A. R. Kay, and D. W. Tank, "Brain magnetic resonance imaging with contrast dependent on blood oxygenation," Proc. Natl. Acad. Sci. U.S.A. **87,** 9868–9872 (1990).
27. G. Fritsch and E. Hitzig, "Über die elektrische Erregbarkheit des Grosshirns," Arch. Anat. Physiol. wissen. Med. **37,** 300–332 (1870).
28. O. Foerster, "Motorische Felder und Bahnen," in *Handbuch der Neurologie,* O. Bumke and O. Foerster, eds. (Springer, 1936).
29. G. Ojemann, J. Ojemann, E. Lettich, and M. Berger, "Cortical language localization inleft, dominant hemisphere. An electrical stimulation mapping investigation in 117 patients," J. Neurosurg. **71,** 316–326 (1989).
30. W. Penfield, "The circulation of the epileptic brain," Res. Publ. Assoc. Res. Nerv. Ment. Dis. **18,** 605–637 (1937).
31. S. S. Kety, "Circulation and metabolism of the human brain," Brain Res. Bull. **50,** 415–416 (1999).
32. M. E. Raichle, "Functional brain imaging and human brain function," J. Neurosci. **23,** 3959–3962 (2003).
33. N. K. Logothetis, "The underpinnings of the BOLD functional magnetic resonance imaging signal," J. Neurosci. **23,** 3963–3971 (2003).
34. T. A. Woolsey, L. Wei, and J. P. Erinjeri, "Dynamic measurements of local cerebral blood flow: examples from rodent whisker barrel cortex," in *Brain Mapping: the Methodology,* 2nd ed., A. W. Toga and J. C. Mazziota, eds. (Academic, 2002), pp. 159–173.
35. A. Grinvald, E. Lieke, R. D. Frostig, C. D. Gilbert, and T. N. Wiesel, "Functional architecture of cortex revealed by optical imaging of intrinsic signals," Nature **324,** 361–364 (1986).
36. D. Malonek and A. Grinvald, "Interactions between electrical activity and cortical microcirculation revealed by imaging spectroscopy: implications for functional brain mapping," Science **272,** 551–554 (1996).
37. M. Wong-Riley, "Changes in the visual system of monocularly

sutured or enucleated cats demonstrable with cytochrome oxidase histochemistry," Brain Res. **171,** 11–28 (1979).
38. S. B. Cox, T. A. Woolsey, and C. M. Rovainen, "Localized dynamic changes in cortical blood flow with whisker stimulation corresponds to matched vascular and neuronal architecture of rat barrels," J. Cereb. Blood Flow Metab. **13,** 899–913 (1993).
39. J. A. O'Sullivan, R. E. Blahut, and D. L. Snyder, "Information theoretic image formation," IEEE Trans. Inf. Theory **44,** 2094–2123 (1998).
40. J. A. O'Sullivan, R. E. Blahut, and D. L. Snyder, "Information theoretic image formation," in *Information Theory: 50 Years of Discovery,* S. Verdú and S. W. McLaughlin, eds. (IEEE, 2000), pp. 50–79.
41. D. L. Snyder, T. J. Schulz, and J. A. O'Sullivan, "Deblurring subject to nonnegativity constraints," IEEE Trans. Signal Proces. **40,** 1143–1150 (1992).
42. I. Csiszár, "Why least squares and maximum entropy? An axiomatic approach to inference for linear inverse problems," Ann. Stat. **19,** 2032–2066 (1991).
43. T. A. Woolsey, "Barrel cortex," in *http://www.ibro.org/Pub_Main_Display.asp?Main ID=21,* (2004).
44. J. P. Erinjeri, "Mechanisms of cerebrovascular regulation in mouse barrel cortex observed with optical imaging," Ph.D. dissertation (Washington University, St. Louis, Missouri, 2002).
45. G. G. Blasdel and S. G, "Voltage-sensitive dyes reveal a modular organization in monkey striate cortex," Nature **321,** 579–585 (1986).
46. M. M. Haglund, G. A. Ojemann, and D. W. Hochman, "Optical imaging of epileptiform and functional activity in human cerebral cortex," Nature **358,** 668–671 (1992).
47. C. J. Hodge, Jr., R. T. Stevens, H. Newman, J. Merola, and C. Chu, "Identification of functioning cortex using cortical optical imaging," Neurosurgery **41,** 1137–1144 (1997).
48. N. Pouratian, S. A. Sheth, N. A. Martin, and A. W. Toga, "Shedding light on brain mapping: advances in human optical imaging," Trends Neurosci. **26,** 277–282 (2003).
49. A. Papoulis and S. U. Pillai, *Probability, Random Variables, and Stochastic Processes,* 4th ed. (McGraw-Hill, 2002), p. 852.
50. D. L. Snyder, J. A. O'Sullivan, D. R. Fuhrmann, and W. H. Smith, "Estimation of overlapping spectral signatures from hyperspectral data," in *Automatic Target Recognition IX.,* F. A. Sadjadi, ed., Proc. SPIE **3718,** 470–479 (1999).
51. D. R. Fuhrmann, C. Preza, J. A. O'Sullivan, D. L. Snyder, and W. H. Smith, "Spectrum estimation from quantum-limited interferograms," IEEE Trans. Signal Process. **52,** 950–961 (2004).